Journal of Applied Fluid Mechanics, Vol. 16, No. 4, pp. 778-793, 2023.
Available online at www.jafmonline.net, ISSN 1735-3572, EISSN 1735-3645.
https://doi.org/10.47176/jafm.16.04.1487

Mechanism of Microbubbles and Cavitation Effect on Bubble Breakage in a Venturi Bubble Generator

Q. Li†, X. Guo, J. Zhang, M. Lei, J. L. Liu, D. Z. Ming and L. Fang

College of New Energy, China University of Petroleum (East China), Qingdao, Shandong, China.

†*Corresponding Author Email: liqiangsydx@163.com*

(Received August 4, 2022; accepted December 14, 2022)

ABSTRACT

Venturi bubble generators have been extensively studied because of having a simple structure and high foaming efficiency, while producing a uniform bubble size. The effect of a noncondensable gas on hydraulic cavitation was considered to improve the Zwart-Gerber-Belamri cavitation model. This improved model and a population balance model were used to study the effect of cavitation on bubble fragmentation. The CFD-PBM results were compared with experimental results, and the accuracy of the improved calculation method was verified in terms of the distributions for the cavitation cavity, gas phase, and bubble size. The calculation results showed that increasing the noncondensable gas content over a certain range promoted the development of hydraulic cavitation, and the cavitation intensity could be indirectly controlled by adjusting the noncondensable gas content. With increasing cavitation intensity, the average bubble size decreased, and the bubble size distribution became narrower. Therefore, a high-pressure pulse generated by cavitation could effectively break bubbles. The development process of microbubbles was studied. The main controlling factors for bubble formation were determined to be the turbulent shear force of the fluid and the collapse impact force of the cavitation group, which provides a theoretical basis for optimizing the design of bubble generators.

Keywords: Microbubble generator; Hydraulic cavitation; Population balance model; Bubble size distribution.

NOMENCLATURE

B_b	growth rate of the number of bubblesdue to fragmentation	P_{sat}	liquid saturation vapor pressure
B_c	growth rate of the number of bubbles due to coalescence	P_V	pressure in bubble
D_b	extinction rate of the number of bubbles due to fragmentation	R_B	radius of single bubble
D_c	extinction rate of the number of bubbles	R_c	condensation rate per unit volume
F_c	condensation coefficient per unit volume	R_e	vaporization rate per unit volume
F_v	evaporation coefficient per unit volume	R_n	total mass transfer rate per unit volume
f_g	mass fraction of NCG	v_m	velocity of mixture phase
k	turbulent kinetic energy	α_v	volume fraction of vapor
		ρ_m	density of mixture phase
		μ_m	dynamic viscosity
		ρ_n	bubbles number density
		ρ_V	vapor phase density

1. INTRODUCTION

A bubble generator breaks gas into microbubbles through the action of turbulent shear by a liquid on a gas (Watarai 2011). Compared with traditional bubbles, micro/nanobubbles (0.01~100 μm) are characterized by a slow rising speed, long residence time, and large gas–liquid contact area (Juwana *et al.* 2018), which can effectively enhance the gas–liquid two-phase mass transfer process and reduce operating costs (Kawashima 2000; Parmar and Majumder 2013). To develop a bubble generator with excellent performance and a simple structure, considerable research has been performed on bubble generator mechanisms (Uchiyama *et al.* 2018; Brasileiro *et al.* 2019). Yin *et al.* (2015) experimentally studied the development of the bubble size in a Venturi bubble generator (VBG) and found a linear relationship between the bubble size and gas volume ratio. Nao-Aki *et al.* (2020) studied

the effect of the shear stress on bubble breakage and designed a honeycomb bubble generator. Researchers at Oak Ridge National Laboratory carried out experimental studies on different types of bubble generators and found that that a simple structure makes the VBG highly feasible for application; thus, several types of VBG-based bubble generators were designed (Flynn and Deboisblac 1966). Huang showed that the VBG performance depends on the mechanical structure and working conditions of a bubble generator, which together determine the bubble size distribution (Huang *et al.* 2020).

The average bubble size is an important parameter for characterizing the performance of a bubble generator. Serizawa (2003) designed a VBG that can produce bubbles with an average size of 72.2 μm. Tabei *et al.* (2007) carried out experimental and numerical simulation studies on the hydraulic characteristics of bubble generators with strong swirl jets and found an average microbubble size of 48.8 μm was produced. Sadatomi *et al.* (2012) constructed a multifluid mixer from a simple combination of porous tubes and orifice plates that produced microbubbles with an average size of 120 μm. The bubble size distribution is also an important factor for improving the process efficiency, which is influenced by the structural design and operating conditions of the bubble generator (Rezai and Koleini 2008). Gordiychuk *et al.* (2016) used a postprocessing algorithm to extract data from experimental videos and discussed the significance of the bubble size distribution. Kim *et al.* (2019) designed a novel swirling microbubble generator for a system for multistage direct contact membrane distillation and desalination and characterized the effect of the bubble size distribution on the bubble generator performance.

During the formation of micro/nanobubbles, the throat of the VBG exhibits a negative pressure below the saturated vapor pressure, such that a cavitation cavity forms in the back and divergent sections of the throat (Li *et al.* 2017; Cai *et al.* 2019) and the pressure pulsation caused by the cavitation effect can break bubbles around the throat (*Dular and Coutier-Delgosha* 2013). Deng *et al.* (2020) used atomic force microscopy to observe how micron-sized bubbles generated by the cavitation effect promoted flotation. Therefore, hydraulic cavitation is also a key factor in the formation of micro/nanobubbles.

The presence and influence of a noncondensable gas (NCG) in a liquid are often overlooked in cavitation studies. The presence of an NCG changes the cavitation characteristics in the flow field, which considerably affects the performance of the equipment used (Sun *et al.* 2019; Braun and Hannon 2010). The presence of NCGs affects the initial volume of the liquid gas core (Briggs 1950), thereby affecting the formation, collapse, and shedding of cavitation bubbles in a fluid (Dilip *et al.* 2018; Yan *et al.* 2018; Baidakov and Vinogradov 2019). Prosperetti (2017) experimentally determined that, in the presence of an NCG, the formation rate of cavitation bubbles increased with the gas core content in water and ultimately reached a fixed value. The NCG significantly changed the fluid collapse dynamics, and bubbles collapsed sharply beyond an NCG content of 2% (Dharmadhikari *et al.* 2011).

In experimental studies, the similarity between the microscopic phenomena of bubble collapse and cavitation collapse make it very challenging to elucidate the mechanism of bubble collapse (Kazakis *et al.* 2008). Thus, numerical simulations and experiments are combined in this study. The Zwart-Gerber-Belamri (ZGB) cavitation model is improved by considering the effect of an NCG on cavitation. This improved ZGB model and a population balance model (PBM) are used to analyze the effects of cavitation on the processes of bubble breakage and microbubble development in the divergent section of a VBG.

2. NUMERICAL SIMULATION METHOD

2.1 Governing Equation

The horizontal flow of a gas–liquid mixture in a venturi tube corresponds to a stable and uniform foam flow. Li *et al.* (2011) found that the slip velocity is negligible for bubble sizes below 0.1 mm or fluid flow velocities above 0.1 m/s. Therefore, assuming that the gas and liquid phases in the flow field are completely mixed, a transport equation for the mixture can be obtained by neglecting the effect of the slip velocity between the two phases. The continuity equation and momentum equation are given below:

$$\frac{\partial \rho_m}{\partial t}+\frac{\partial\left(\rho_m u_j\right)}{\partial x_j}=0 \tag{1}$$

$$\begin{aligned}&\frac{\partial\left(\rho_m v_m\right)}{\partial t}+\nabla\cdot\left(\rho_m v_m v_m\right)\\&=-\nabla P+\nabla\cdot\left[\mu_m\left(\nabla v_m+\nabla v_m^T\right)\right]\end{aligned} \tag{2}$$

where v_m and ρ_m are the velocity and the density of the mixture phase, μ_m is the dynamic viscosity, and P is the local pressure.

The continuity equation for the secondary phase can be used to derive the following equation for the volume fraction of the secondary phase:

$$\begin{aligned}&\frac{\partial}{\partial t}\left(\alpha_p\rho_p\right)+\nabla\cdot\left(\alpha_p\rho_p\vec{v}_m\right)\\&=-\nabla\cdot\left(\alpha_p\rho_p\vec{v}_{dr,p}\right)+\sum_{q=1}^{n}\left(\dot{m}_{qp}-\dot{m}_{pq}\right)\end{aligned} \tag{3}$$

where q is the first phase, p is the second phase, $\dot{m}_{qp}$ denotes the mass transfer from phase q to phase p. $\dot{m}_{pq}$ denotes the mass transfer from phase p to phase q.

2.2 Mixture Model

The gas–liquid mixture is described using a simplified multiphase flow model in which the two phases flow at different velocities. In the model, the phases are allowed to interleave with each other and are strongly coupled. A uniform multiphase flow can be simulated with a constant velocity for each phase and strong coupling between phases. This hybrid model offers the advantages of having a simple structure, requiring low computational effort for solution and producing relatively reliable results. The mixture model is the best choice for systems in which the interphase traction cannot be easily measured. The mixture model is convenient and fast to use for studying systems in which the distribution of dispersed phases is not concentrated, such as a gas–liquid mixed flow in a bubble generator, for which the bubble distribution is highly scattered.

2.3 Improved Cavitation Model

Cavitation models that are commonly used include the ZGB, Schnerr-Sauer and full cavitation models (Yang *et al.* 2013). The ZGB model can capture the details of a cavitation flow field and is more suitable for numerical simulation of a Venturi tube than other models (Li *et al.* 2018). However, the effect of an NCG on the cavitation flow field is not considered in deriving the ZGB model. Therefore, in this study, the presence of an NCG is incorporated into the ZGB cavitation model. This improved cavitation model is used to analyze the effect of the NCG content on the cavitation intensity in the bubble generator.

The vapor volume fraction α_v can be expressed as the product of the bubble number density ρ_n and the volume of a single bubble as follows:

$$\alpha_V = \rho_n \cdot \left(\frac{4}{3} \pi R_B^3 \right) \tag{4}$$

where R_B is the radius of a single bubble.

The interphase mass transfer rate per unit volume of vapor R_n is the product of the mass of a single bubble and the number density of bubbles (assuming that all the bubbles have the same size):

$$\overset{\square}{R}_n = \rho_n \cdot \left(4\pi R_B^2 \rho_V \frac{\mathrm{d}R_B}{\mathrm{d}t} \right) \tag{5}$$

where ρ_V is the density of the vapor phase.

The relationship between the change in the bubble radius and the pressure is given below.

$$\frac{\mathrm{d}R_B}{\mathrm{d}t} = \pm \sqrt{\frac{2}{3} \frac{|P_v - P|}{\rho_l}} \tag{6}$$

Substituting Eq. (4) and Eq. (6) into Eq. (5) yields the following expression for the net mass transfer:

$$\overset{\square}{R}_n = \frac{3\alpha_V \rho_V}{R_B} \sqrt{\frac{2}{3} \frac{P_V - P}{\rho_l}} \tag{7}$$

where P_V is the interior pressure of the bubbles.

The presence of an NCG is incorporated into the ZGB model (Singhal *et al.* 2002) as follows:

$$\begin{cases} R_e = F_v \dfrac{3\alpha_{nuc}\left(1-\alpha_V-\alpha_g\right)\rho_V}{R_B} \sqrt{\dfrac{2}{3}\dfrac{P_V - P}{\rho_l}} & \left(P \le P_V\right) \\ R_c = F_c \dfrac{3\alpha_V \rho_V}{R_B} \sqrt{\dfrac{2}{3}\dfrac{P - P_V}{\rho_l}} & \left(P \ge P_V\right) \end{cases} \tag{8}$$

where R_c and R_e are the condensation and vaporization rates per unit volume, respectively; F_v and F_c are the evaporation coefficient and condensation coefficient per unit volume, respectively; and P_V is the interior pressure of a bubble and is expressed as

$$P_v = P_{sat} + 0.195\rho_m \cdot k \tag{9}$$

where k is the turbulence intensity.

The density of a mixture with an NCG becomes:

$$\rho_m = \left[\alpha_V \rho_V + \left(1-\alpha_V-\alpha_g\right)\rho_l\right] / \left(1-f_g\right) \tag{10}$$

where f_g is the NCG mass fraction and α_v is the volume fraction of the vapor.

Antoine's formula is introduced to accurately account for the temperature dependence of the saturated vapor pressure of the water vapor (Wagner 1973; Wisniak 2001; Drioli and Giorno 2016).

$$log P_{sat} = \mathrm{A}\text{-}\mathrm{B}/\left(\mathrm{T}\text{-}273.15+\mathrm{C}\right) \tag{11}$$

A, B, and C are empirical parameters with values of 8.10765, 1750.286, and 235, respectively, over a temperature range of 10 °C to 55 °C.

2.4 Population Balance Model

Under general conditions, the particles constituting a phase are characterized by a size distribution. The size of these particles, such as solid particles, droplets, bubbles, etc., changes with time. The bubbles in the bubble generator undergo nucleation, growth, coalescence, and fragmentation (Wencai *et al.* 2014). Therefore, in addition to the basic energy conservation equation, an equation must be derived to describe the equilibrium between particles in multiphase flow. This equilibrium equation is derived within the PBM framework. The PBM includes a bubble coalescence model and crushing model.

The PBM can be expressed as follows:

$$\frac{\partial}{\partial t}\left[n(v,t)\right]+\nabla\cdot\left[\vec{u}n(v,t)\right]=S(v,t) \quad (12)$$

where v is the original bubble volume, t is the time, n is a bubble number density function, and $S(v, t)$ is a source term for bubble coalescence and breakage, which can be expressed as (Zhang and Li 2020):

$$S(v,t)=B_c(v,t)-D_c(v,t)+B_b(v,t)-D_b(v,t) \quad (13)$$

$$B_c=\frac{1}{2}\int_0^v a(v-v',v')n(v-v',t)n(v',t)dv' \quad (14)$$

$$D_c=\int_0^\infty a(v,v')n(v,t)n(v')dv' \quad (15)$$

$$B_b=\int_V^\infty g(v')\beta(v,v')n(v',t)dv' \quad (16)$$

$$D_b=g(v)n(v,t) \quad (17)$$

where B_c and D_c are the growth and extinction rates of the number of bubbles due to coalescence, respectively, and B_b and D_b are the growth and extinction rates of the number of bubbles due to fragmentation, respectively. v' is the volume of a sub-bubble. a (v, v') is the coalescence frequency of bubbles with volumes between v and v'; $g(v)$ is the breaking frequency of a bubble with a volume v; and $\beta(v, v')$ is the probability density function associated with bubbles with volumes between v and v'.

The bubble aggregation and fragmentation frequencies in the equations are influenced by the bubble size in the multiphase fluid, the density of the two fluids, and Weber's number.

3. NUMERICAL PROCEDURE

3.1 Model Geometry

To produce a large number of tiny bubbles efficiently, increase the sample number and reduce experimental measurement error, the VBG throat structure was redesigned. The bubble generator used in this study is shown in Fig. 1. The dimensions of each part of the 3D model are shown in Table 1.

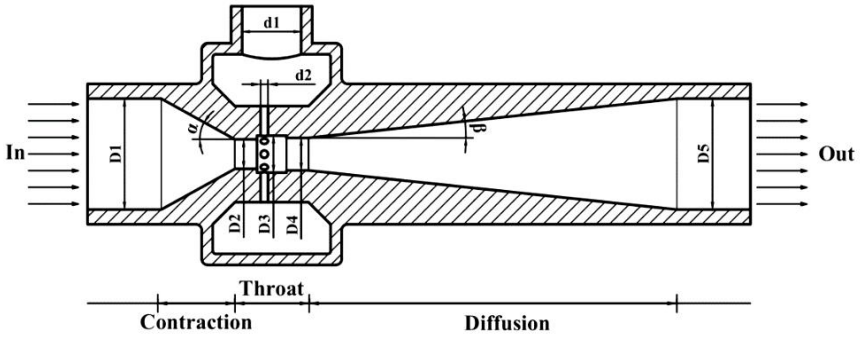

Fig. 1. Model of the bubble generator.

Table 1 Dimensions of different parts of the model.

Serial number	Model part	Dimension (mm/°)
1	Liquid inlet and outlet D1 and D5	15
2	Convergence angle α	25
3	Divergence angle β	6
4	Air inlet port d1	10
5	Air suction port d2	1
6	Throat diameter D2	3.6
7	Throat diameter D3	4.0
8	Throat diameter D4	3.8

3.2. Grid Independence

FLUENT 18.0 was used to simulate and analyze the internal flow field for all calculations. The results of previous studies on grid independence show that the grid resolution significantly affects the distribution of the cavitation flow field, bubble coalescence, and the bubble size distribution (Long *et al.* 2017, 2019). Therefore, the sensitivity of the spatial discretization was investigated based on the flow-field pressure distribution under an inlet/outlet pressure ratio of 0.287. ANSYS MESH was used to mesh the model, and the model was chunked to obtain as many structured meshes as possible; a lower computational error was obtained using a structured mesh than using an unstructured mesh. Considering that three phases meet and mix in the throat, the throat mesh was encrypted to ensure the quality of the mesh. The grid quality was higher than 0.8. Figure 2 is the grid division diagram of the model. The numerical calculations were carried out using 300,000, 400,000, 500,000, and 600,000 grids. The calculation results

are shown in Fig. 3. The pressure distribution did not change beyond 500,000 grids. Thus, 500,000 grids were used to ensure grid quality. X=12 mm corresponds to the throat entrance, and X=22 mm corresponds to the entrance of the divergent section. A comparison of the grid sensitivities of first-order and second-order quantities showed that using the second-order quantity condition increased the calculation accuracy without significantly increasing the computation time; therefore, the second-order quantity was chosen for this study.

To verify the accuracy of the model, the inlet pressure of the bubble generator using different inlet flow rates and an outlet at atmospheric pressure was compared with experimental values. The results are shown in Fig. 4. The same trend is observed for the inlet pressure determined by both experiment and simulation, and the maximum error does not exceed 10%, which is acceptable for multiphase flow simulation results and effectively verifies the accuracy of the model.

3.3 Boundary Conditions and Solution Methods

Changes in the flow rate significantly affect the performance of a bubble generator. The liquid flow rate was set at 1.0 m^3/h, and the gas flow rate was maintained at 0.02-0.05 m^3/h. The gas–liquid ratio was changed by adjusting the gas inlet flow rate. The outlet pressure was set at 0.1 MPa. Second-order upwind discretization was used to increase the accuracy of the calculation of the turbulent kinetic energy and turbulent energy dissipation rate. The SIMPLEC algorithm was used to calculate the coupling of the pressure and velocity in the flow field, and the PRESTO! format was used to present the differential pressure value. The RNG k-ε turbulence model, which is suitable for fast strain medium vortices and local complex shear flow, was used as the turbulence model. The time step was 0.00001 s.

Functions for bubble coalescence and fragmentation must be given to solve the PBM of a gas–liquid system and are key to accurately predicting the bubble size distribution in a liquid. Figure 5 compares the bubble size distribution obtained using different models with experimental data. Both the average bubble size and bubble size distribution obtained using the Luo and free Luo models were found to be inconsistent with the experimental data. The bubble sizes obtained using the Tur–Luo model were between 20 and 80 μm, and the corresponding average bubble size was approximately 51 μm, which was slightly smaller than the experimental size of 56 μm. The experimentally determined bubble size was based on images from drainage tests, where bubble aggregation occurs in a drainage pipe. Therefore, the bubble size distribution measured by image analysis is slightly larger than the actual bubble size distribution at the exit. Therefore, the results of the turbulent convergence model and Luo fragmentation model are consistent with the experimental data. The Tur–Luo model was thus used to describe bubble breakage in the analysis presented below.

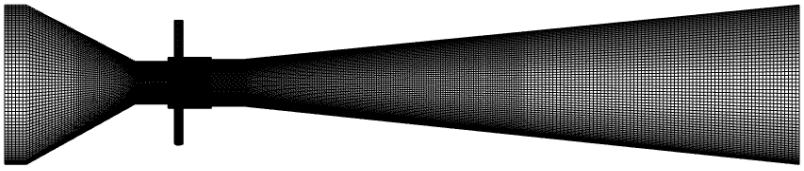

Fig. 2. Generation of the mesh for the model.

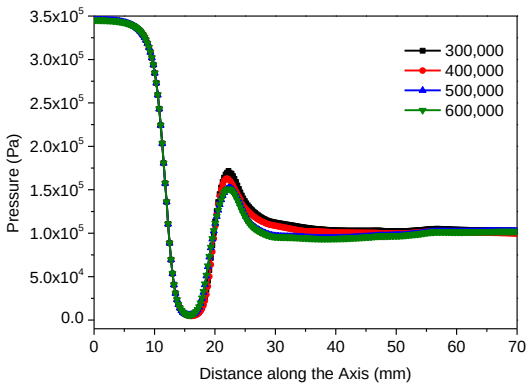

Fig. 3. Grid sensitivity analysis of the CFD simulation.

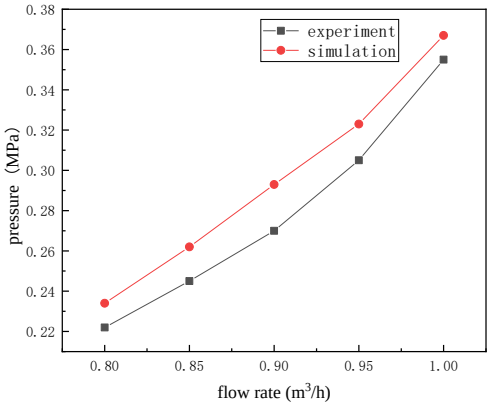

Fig. 4. Comparison of inlet pressures obtained using simulation and experiment.

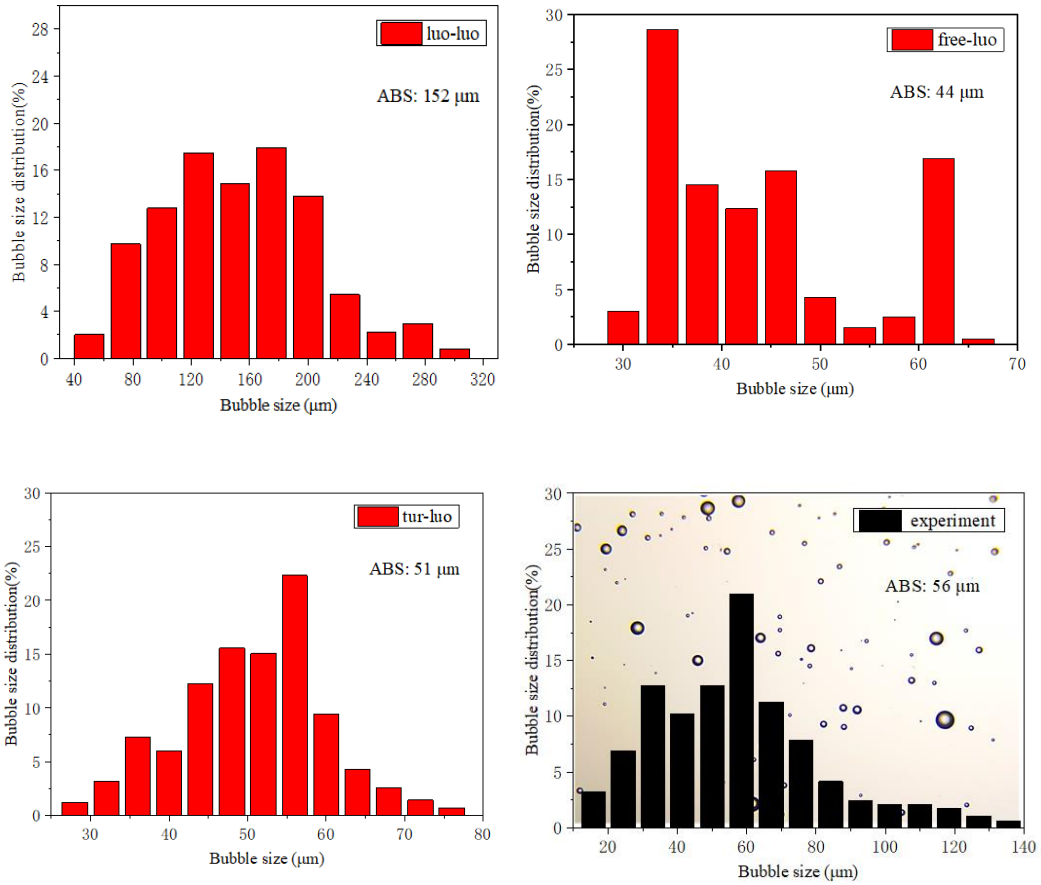

Fig. 5. Comparison between results obtained from PBM calculations and experiments.

3.4 Experimental Device

Figure 6 shows the platform used to test the VBG performance, which comprises a microbubble visual observation system, a gas–liquid drainage system, a bubble observation and treatment system, and fluid delivery pipelines and control components. The microbubble generation system includes a transparent VBG for flow visualization, centrifugal pump, liquid turbine flowmeter, and gas flowmeter. The bubble observation and processing system includes a bubble observation tank, microscope, computer image recording system, and MATLAB postprocessing program. We used a Phenix PH50 microscope, a frame rate of 2.7 during shooting, an exposure time of 350 ms, and a lens magnification of 40. Table 2 shows the average particle size and relative deviation determined from four groups of measurements made under the same conditions, where more than 1000 bubbles were collected in each group of experiments. The results show that the relative deviation in the average particle size measured in each group is less than 10%, effectively verifing the experimental reproducibility.

3.5 Image Postprocessing

A mixture of bubbles and water is introduced into the bubble observation tank via the drainage system, the bubble image is obtained by microscope amplification, and then an image is collected by the computer connected to the microscope. The MATLAB program is used to perform image correction, image segmentation, particle counting, and image restoration, and the bubbles in the image are processed into clear, independent, and nonoverlapping bubble groups. Finally, the bubble particle size is measured. The processing process is shown in Fig. 7. A binarization image is generated, the number of pixels is accumulated, and the bubble

Table 2 Measured mean bubble diameters and calculated relative deviation

Experiment No.	1	2	3	4	Mean
Bubble diameter/μm	58.16	53.49	60.32	54.76	56.68
Relative deviation/%	2.61	5.62	6.42	3.39	4.51

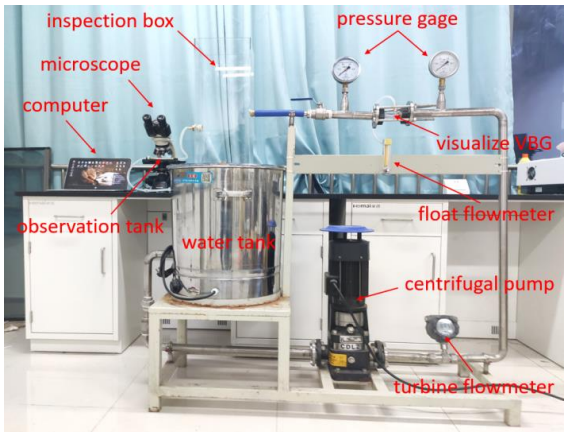

(a) The experimental device

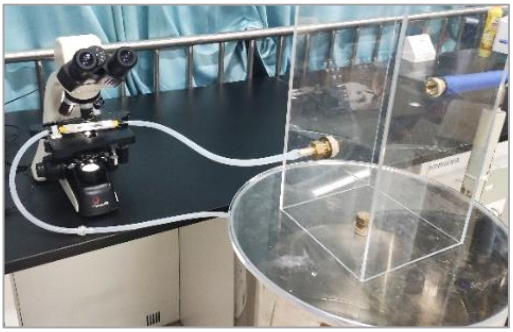

(b) Microbubble measurement system

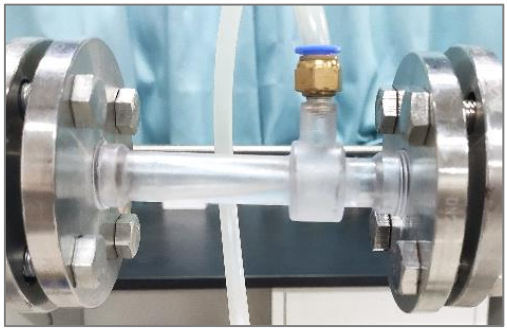

(c) Visual observation system

Fig. 6. Platform used to test the VBG performance.

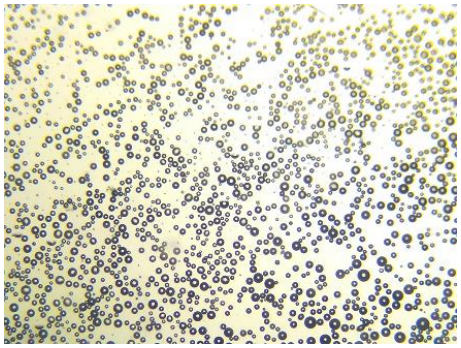

(a) image correction

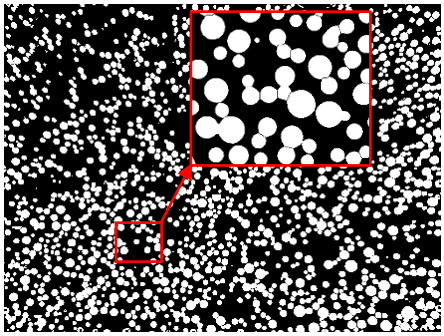

(b) image segmentation

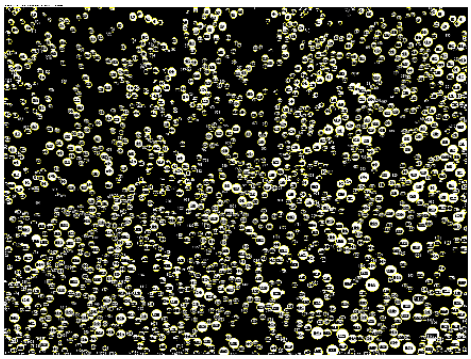

(c) particle counting

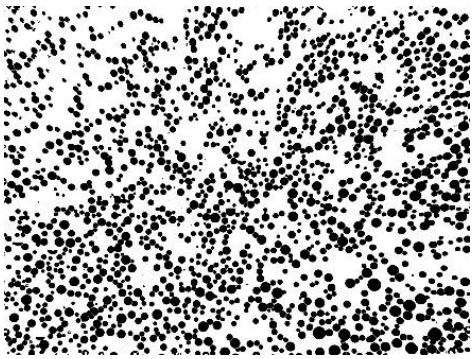

(d) image restoration

Fig. 7. Image postprocessing.

diameter d_b is calculated. The calculation formula is as follows:

$$d_b = \sqrt{\frac{4n_p S_P}{\pi}} \tag{18}$$

where n_p is the number of pixel points occupied by a single bubble, and S_p is the area of a single pixel point. The average bubble diameter corresponds to the Salter average diameter given below.

$$d_{32} = \frac{\sum_{i=1}^{n} d_i^3}{\sum_{i=1}^{n} d_i^2} \tag{19}$$

To reduce accidental error and ensure measurement accuracy, no fewer than 1000 bubbles were measuredunder each experimental condition. A novel image processing method based on deep learning for bubble detection, segmentation, and shape reconstruction was developed to characterize submillimeter bubbly flows with high gas holdup (Cui *et al*. 2022). This method can characterize submillimeter bubbly flows with gas holdups of up to 20%.

4. RESULTS AND DISCUSSION

4.1 Comparison of Simulation and Experimental Results

The reliability of the numerical simulation results for the VBG were verified against the experimental results. The verification parameters were the cavitation cavity length, gas phase distribution, and bubble size distribution.

First, the cavitation cavity length parameters of the VBG were verified. To eliminate the effect of air on the results and facilitate observation of cavitation in the throat, a venturi tube with the same structural parameters but no air intake was adopted. The cavity distribution were obtained from the numerical simulation and experiment under the same working conditions. Figure 8 shows the images obtained from the simulation and experiment that were grayed out using MATLAB software.

Cavitation groups refract light to create dark areas. When the cavitation collapses, the gas–liquid mixture formed appears as a gray area. The more bubbles there are in a cavity, the darker the cavity appears. The same locations in the simulation and experimental results are cut off and grayed in Fig. 8. Then, the gray values of the simulation and experimental results are extracted after grayscale processing, and the axial location (X) is dimensionalized by the length of the diverging section (L), as shown in Fig. 9 (the experimental data presented were obtained by Qiang Li (Li *et al*. 2020). The lowest gray value and the maximum volume fraction of the vapor phase are obtained at X/L=0.15. Compared with the results obtained using ZGB model, the results of the numerical simulation in the presence of an NCG exhibit a clear gradient. Combining the results presented in Figs. 8 and 9 shows that the gradient corresponds to the falling off and collapse of a captured cavitation bubble, and the gray fitting curve obtained using the improved model is closer to the experimental data than that obtained using the ZGB model.

The parameters for the gas phase distribution of the VBG were verified by comparing the gas phase distribution obtained by experiment and simulation,

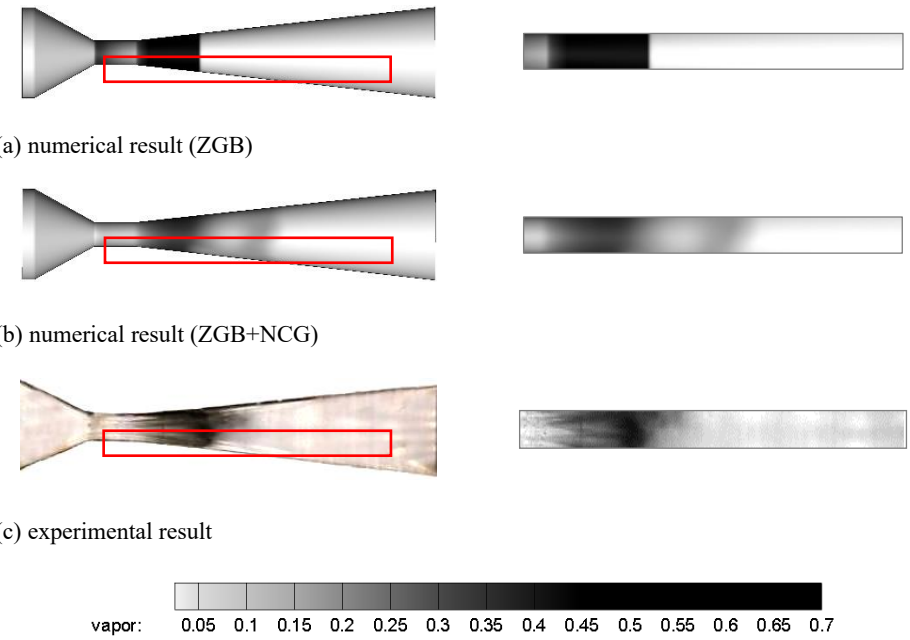

Fig. 8. Gray processing of simulated and experimental results (vapor).

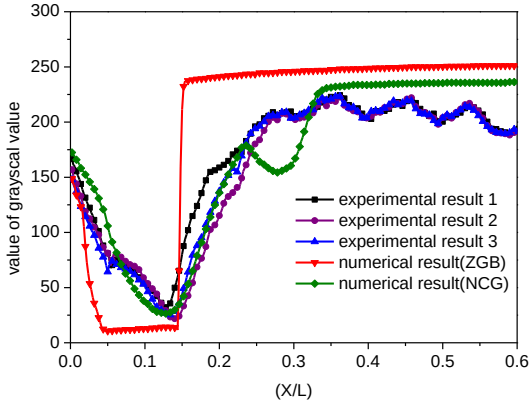

Fig. 9 Comparison between experimental and simulation results.

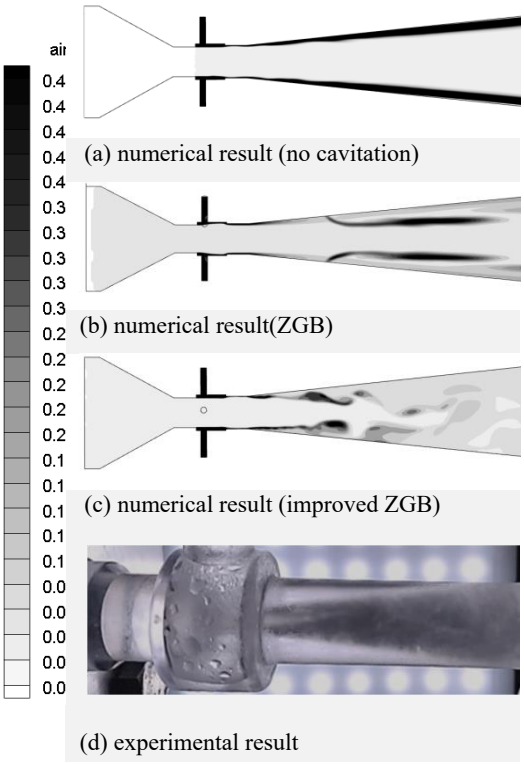

Fig. 10. Gray processing of simulated and experimental Results air).

as shown in Fig. 10. In the absence of cavitation, the gas phase is mainly distributed on the divergent wall surface, resulting in a wall attachment effect (the Coanda effect). The Coanda effect of gas is partially eliminated In the ZGB model due to the effect of cavitation. However, gas-phase aggregation still occurs, which prevents effective breakage of bubbles. In the improved ZGB model, the gas phase bubbles are gradually broken and dispersed from the throat to the divergent section, and a uniform gas–liquid mixture is formed at the exit. The simulation results obtained using the improved ZGB model are consistent with the experimental image.

Figure 11 is a comparison of the bubble size distributions obtained by experiment and simulation, and Table 3 shows the average bubble size obtained under four conditions (a) ~ (d).

Figure 11 shows that the bubble size distribution measured in the experiment is 10-140 μm. In the absence of a cavitation model, the bubble size range is 80-180 μm, which is significantly larger than the experimental results. This result indicates that a larger particle size is obtained by considering only turbulent broken bubbles and the effect of cavitation on bubble crushing must be considered. The bubble size range obtained by numerical simulation of the ZGB cavitation model is 20-70 μm, with almost zero bubbles in the range of 24 to 34 μm. In practice, the bubble size distribution is close to a normal distribution and tends to have a single dominant size. Thus, the simulation results obtained using the ZGB cavitation model do not follow a normal distribution, indicating an unrealistic bubble size distribution. The simulation results obtained using the ZGB model incorporated with an NCG indicate a bubble size range of 20-100 μm, which is more consistent with the experimental results than the aforementioned simulation results. The same conclusions can be drawn using the average bubble size presented in Table 3.

Table 3 Experimental and simulated average bubble size.

Cavitation Model	(a)	(b)	(c)	(d)
Average bubble size (μm)	57.01	112.51	45.72	56.34

4.2 Influence of the Inlet Flow Rate on the Bubble Size

The experimental results show that the liquid inlet flow rate and the gas–liquid ratio have a significant influence on the bubble size distribution, where different combinations of air and water flow rates produce bubble size distribution curves with specific characteristics. Therefore, it is necessary to study the influence of the liquid flow rate on the bubble size distribution. The bubble crushing performance can be characterized by two parameters: the average bubble size and the corresponding standard deviation. The average bubble size is a measure of the ability of the VBG to break bubbles. The standard deviation in the bubble size reflects the range of bubble sizes and indirectly represents the uniformity of the particle size. Expressions for these two parameters are given below.

$$\bar{Q}=\frac{Q_1+Q_2+\cdots+Q_n}{n} \tag{20}$$

$$\sigma(q)=\sqrt{\frac{1}{n-1}\sum_{i=1}^{n}(q_i-\bar{q})^2} \tag{21}$$

Figure 12 shows the average bubble size and corresponding standard deviation at water flow rates

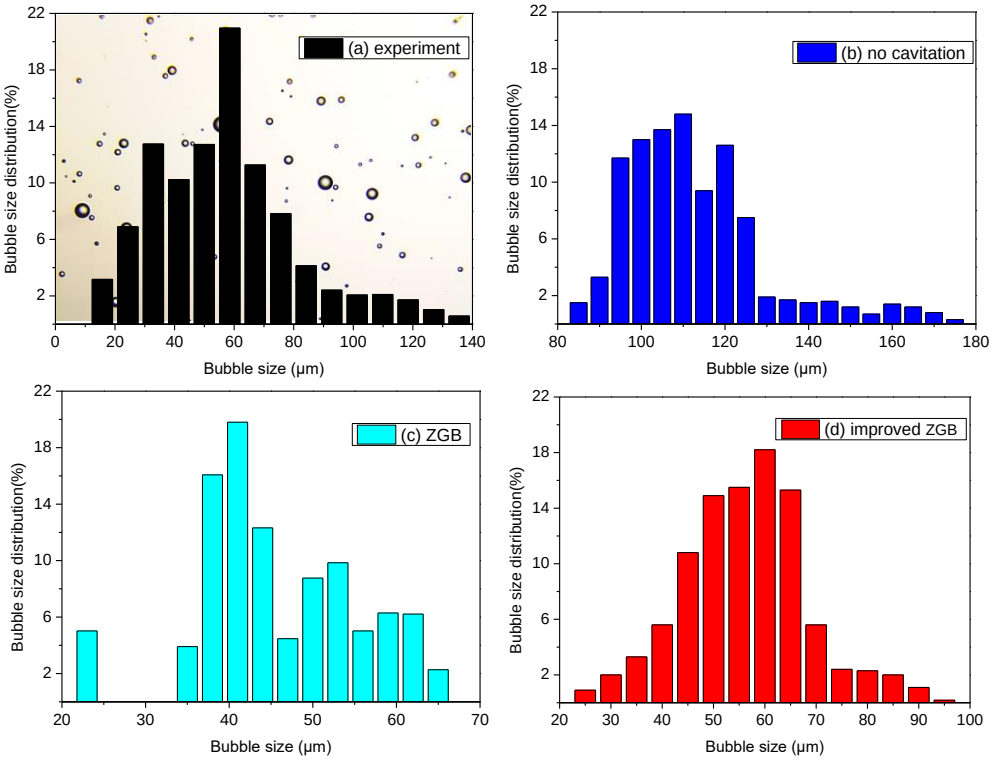

Fig. 11. Experimental and simulated bubble size distribution.

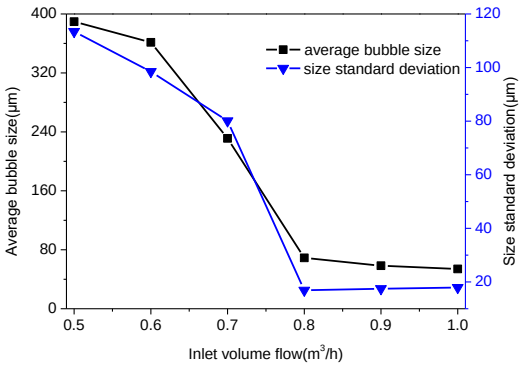

Fig. 12. Average bubble size and corresponding standard deviation at different flow rates.

of 0.5, 0.6, 0.7, 0.8, 0.9, and 1.0 m^3/h at a gas–liquid ratio of 2%. With increasing liquid inlet flow, both the average bubble size and corresponding standard deviation trend sharply downward and then remain stable. Both parameters have turning points at 0.8 m^3/h, at which the bubble particle size and bubble size distribution range are significantly reduced. Figure 13 shows the bubble size distribution at flow rates of 0.7 and 0.8 m^3/h. At flow rates below 0.8 m^3/h, the span of bubble sizes exceeds 300 μm, and the average bubble size and corresponding standard deviation are 361 μm and 231 μm, respectively. At flow rates above 0.8 m^3/h, the average bubble size of the bubbles decreases sharply to 58 μm and 54 μm, and the standard deviation in the bubble size decreases from 98 μm and 80 μm to approximately 17 μm.

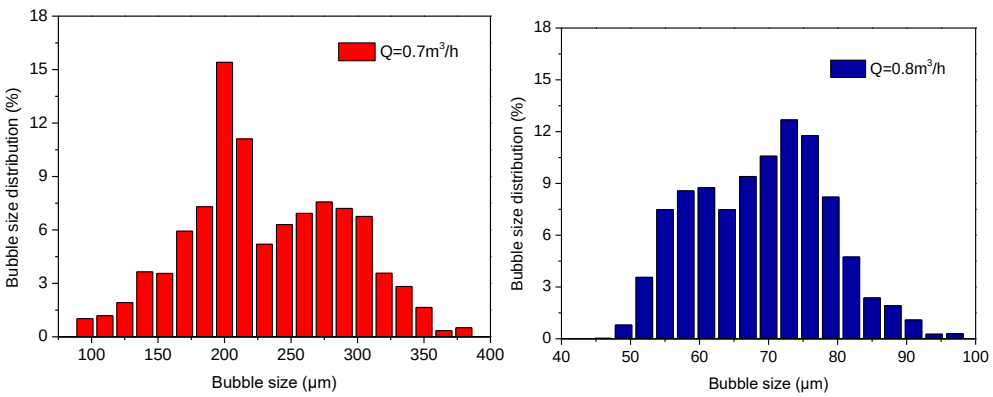

Fig. 13. Bubble size distribution at different flow rates.

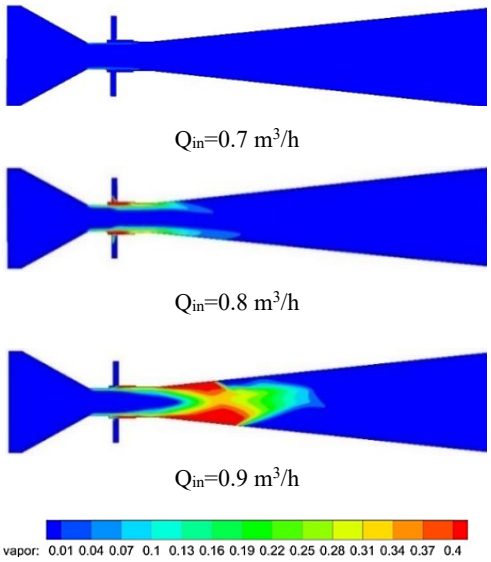

Fig. 14. Vapor phase distribution at different flow rates.

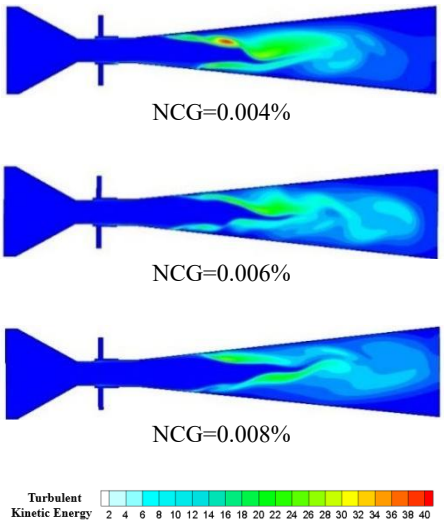

Fig. 15. Turbulent kinetic energy distribution for different NCG contents.

For water flow rates in the range of 0.6-1.0 m^3/h, there is no apparent abrupt change in the pressure distribution, flow velocity distribution, and turbulence intensity, but the cavitation cavity starts to form at 0.8 m^3/h. A different phenomenon from the formation of a gradient in the flow velocity occurs: when the throat flow velocity increases from 16.1 m/s to 18.5 m/s, a cavitation cloud suddenly appears and rapidly expands, forming cavitation clouds in the throat and the divergent section of the VBG. Figure 14 shows the vapor phase distribution for water flow rates of 0.7-0.9 m^3/h. At flow rates above 0.8 m^3/h, increasing the flow rate causes the throat pressure to drop below the saturated vapor pressure, and prominent cavitation clouds are generated near the throat.

Therefore, the sudden change in the bubble size induced by changing the flow rate is mainly caused by the secondary crushing of the bubble group by the impact force generated at the moment of collapse of the cavitation bubble.

4.3 Effect of the Cavitation Intensity on the Bubble Size

The bubble size decreases abruptly with increasing flow rate because cavitation occurs as the flow velocity increases. However, the change in the flow rate also affects parameters such as the pressure, flow rate, and turbulent kinetic energy of the flow field. Therefore, the influence of cavitation on the bubble particle size needs to be further analyzed.

The influence of the cavitation intensity on the bubble size can be determined by controlling the NCG content in water. An NCG usually exists in water at an extremely low content in the form of tiny cavitation bubbles, which change the cavitation characteristics of the flow field. An NCG has little effect on parameters other than the cavitation flow field and does not affect the fluid characteristics of the bubble generator. For example, changing the NCG content has little effect on the turbulent kinetic energy, which influences bubble fragmentation (as shown in Fig. 15).

The NCG content was set to 0.002%, 0.004%, 0.006%, and 0.008% to investigate the effect of cavitation on the bubble size. Figure 16 shows the vapor phase distribution generated by cavitation in the VBG. When the fluid enters the throat, the cavitation cavity gradually expands from the inner wall of the throat to the central axis and then gradually disappears in the middle of the divergent section with the exfoliation and collapse of the cavitation group.

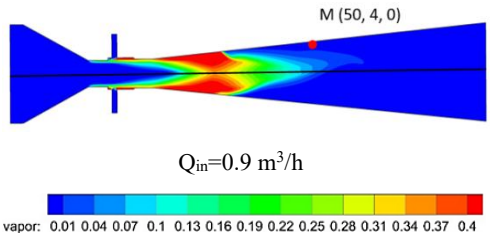

Fig. 16. Schematic of the vapor volume fraction along the central axis.

The volume fraction of the vapor phase along the central axis was extracted to compare the effects of different NCG contents more clearly, and the results are shown in Fig. 17. When the NCG is taken into

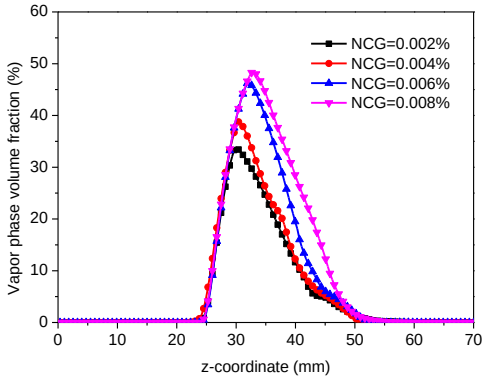

Fig. 17. Effect of the NCG content on the vapor volume fraction.

account, the cavity length does not change significantly after cavitation, but the maximum volume fraction is significantly affected. The vapor volume fraction in the VBG increases with the NCG content. At an NCG content of 0.008%, the vapor volume fraction reaches up to 48.5%, indicating that the presence of the NCG significantly enhances the cavitation intensity without affecting the cavity length.

Figure 18 shows the bubble size distribution for different NCG contents. The minimum bubble particle size is 32 μm at an NCG content of 0.002% and decreases to 20 μm at an NCG content of 0.008%. The minimum bubble size decreases with increasing NCG content, which indicates that increasing the cavitation intensity improves the ability of the fluid to fracture bubbles. The bubble size distribution is processed to obtain the average bubble size and the corresponding standard deviation, which are shown in Fig. 18. When the NCG content increases, the average bubble size decreases, consistent with the conclusion obtained from Fig. 18.

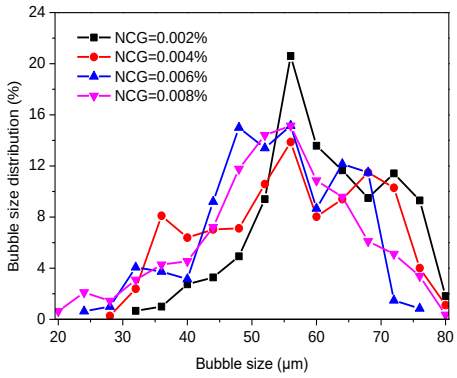

Fig. 18. Bubble size distribution for different NCG contents.

Figure 19 shows that the standard deviation in the bubble size increases slightly with the NCG content.

This result is obtained because increasing the cavitation intensity leads to an increase in the range of bubble sizes. Although the maximum particle size of bubbles for different NCG contents is maintained in the range of 80 μm, the minimum particle size decreases with increasing cavitation intensity, which leads to an increase in the range of bubble sizes and the standard deviation in the bubble size. However, the standard deviation in the bubble size remains stable overall.

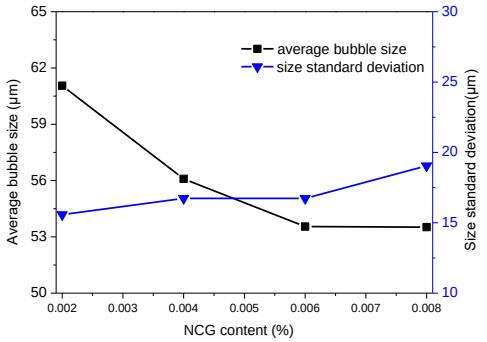

Fig. 19. Average bubble size and corresponding standard deviation for different NCG contents.

Considering that the collapse of the cavity creates a pressure pulsation in the flow field, the time step was adjusted to 1×10^{-6} *s* to effectively capture the pressure change in the flow field. The sampling point M in the divergent section of the VBG is shown in Fig. 16.

Figure 20 shows the pressure pulsation diagram at Point M. Fig. 20(a) shows that the pressure pulsation has excellent periodicity (T). Points a ~ e in Fig. 20(b) correspond to four stages of cavitation development: a primary stage, development, shedding, and collapse. At the monitoring point "d," an extremely strong pressure fluctuation occurs due to the collapse of the cavitation, and the instantaneous pressure peak reaches 1650000 Pa. Finally, the instantaneous high pressure is transmitted as a pressure wave through the flow field and dissipates rapidly. The high-pressure pulsation at the moment of cavitation collapse clearly strongly impacts the nearby bubble, thus producing a good crushing effect on the bubble group.

4.4 Development of Bubbles in Divergent Segments

To explore the process by which the gas is broken into microbubbles, five subsections at equal intervals in the divergent section are selected at the locations shown in Fig. 21. The positions of the five subsections are chosen to follow the developmental process of the cavitation cavity.

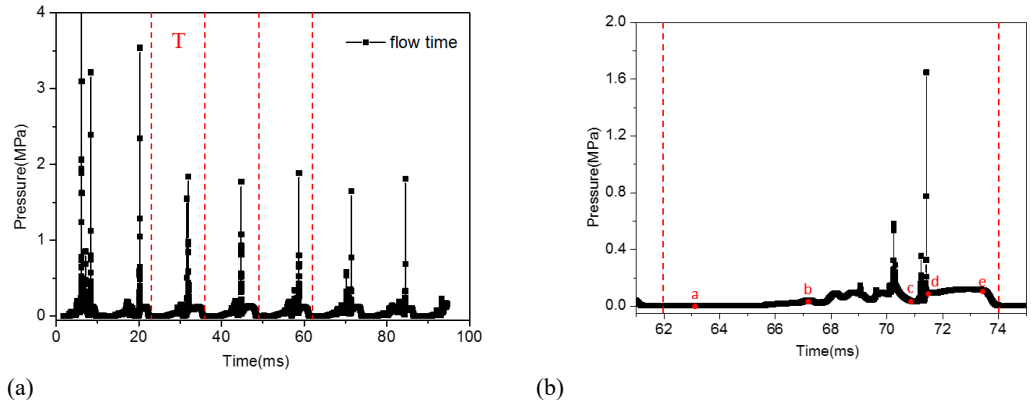

Fig. 20. Time-domain diagram for the pressure pulsation.

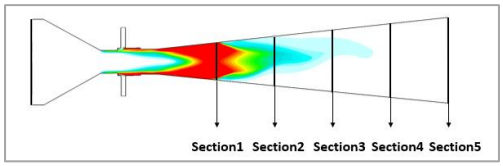

Fig. 21. Schematic showing locations of selected subsections.

The maximum bubble size at Section 1 and Section 2 is over 300 μm. To facilitate comparing the particle sizes via image processing, the bubble size range in the figure is limited to 25-105 μm. That is, bubble diameters larger than 105 μm are treated as 105 μm. The bubble size distribution of the five sections is processed and summarized. Figure 22 shows the bubble size distribution that is used to determine the average bubble size and the corresponding standard deviation shown in Fig. 23.

At Section 1 of the divergent section, nearly 30% of the bubbles are larger than 100 μm in diameter, and a large number of bubbles have diameters above 300 μm. This result indicates that cavities have been formed at Section 1 but all exist as bubbles that have not undergone collapse and breakage: thus, bubbles cannot be broken in Section 1. At the same time, the liquid enters the throat to form a high-speed jet, such that a portion of the gas is sheared into microbubbles. When the gas–liquid mixture reaches Section 2, the cavity is fully developed and begins to fall off and collapse locally. At this time, the bubble size follows a normal distribution and tends to a single dominant size of 72 μm. This result indicates that the turbulent shear force and impact of cavitation collapse in Section 2 affects most of the gas: the average bubble size is further reduced, but large bubbles still remain. When the cavity reaches Section 3, a large area of the cavity has collapsed. At this time, both the average bubble size and corresponding standard deviation significantly decrease. Although the dominant bubble size is still 72 μm, there is a sharp decrease in the number of large bubbles over 100 μm in diameter in the flow field. The bubbles at Section 4 and Section 5 are further broken, and the average bubble size is further reduced.

In conclusion, there are two main factors that control the formation of bubbles in the VBG. First, the turbulent shear force has a strong effect on bubbles. The turbulent flow in the VBG starts from the throat and extends to the entire divergent section. Strong turbulence creates a force in the flow field that shears and breaks bubbles. Second, the impact effect of the

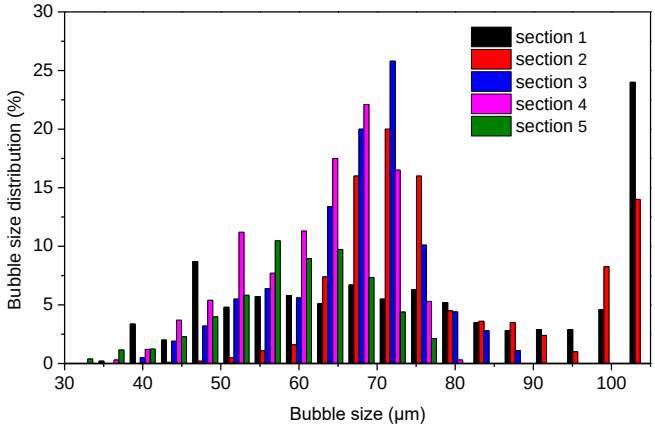

Fig. 22. Bubble size distribution in different sections.

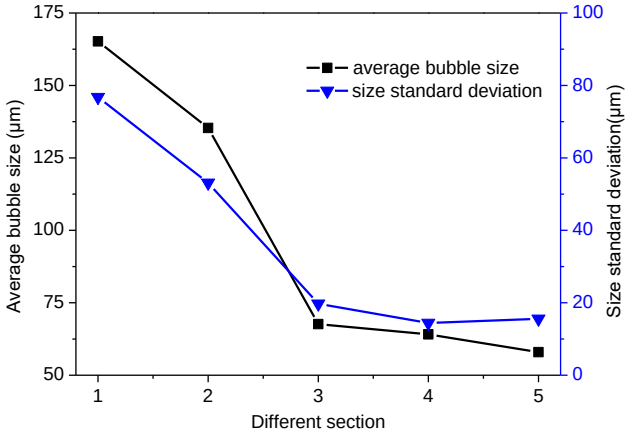

Fig. 23. Average bubble size and corresponding standard deviation in different sections.

cavitation group collapses in the flow field. Gas nuclei are generated rapidly in the water body in the throat and collapse in the divergent section. A large quantity of energy is generated during the process, which has a strong impact on the nearby bubble and a crushing effect on the bubble group.

5. CONCLUSIONS

In this study, a Venturi bubble generator is constructed, and the Zwart-Gerber-Belamri cavitation model is improved and numerically simulated. The numerical simulation is validated by experimental results. The improved Zwart-Gerber-Belamri model is used to analyze the effect of cavitation on the bubble size.

The conclusions drawn from the study are summarized below.

(1) The presence of a noncondensable gas affects the cavitation strength. As the noncondensable gas content increases, the vapor volume fraction increases but the cavity length is not affected.

(2) With increasing liquid flow rate, there is a sudden turning point in the bubble size that is mainly caused by the cavitation effect.

(3) The cavitation strength can affect bubble breakage. As the cavitation strength increases, both the average and minimum bubble particle sizes decrease.

(4) The crushing effect of cavitation on the bubble group mainly depends on the impact of the high-pressure pulsation generated during cavitation collapse, where the instantaneous pressure peak can reach 1650000 Pa.

(5) Bubble breakage occurs mainly in the divergent section of the Venturi bubble generator. The turbulent shear force of the fluid and the impact force of cavitation collapse are the main controlling factors for the formation of micro/nanobubbles.

ACKNOWLEDGEMENTS

Thiswork is supported by the National Natural Science Foundation of China (52176050), the Natural Science Foundation Project of Shandong Province (ZR2020ME174).

REFERENCES

Baidakov, V. G. and V. E. Vinogradov (2019). Limiting stretchings of liquid oxygen: Experiment and classical nucleation theory. *International Journal of Heat & Mass Transfer* 129, 1057-1065.

Brasileiro, P. P. F., L. B. D. Santos, M. J. Chapro, D G. D. Almeida, C. Marcos José, B. A. C. Roque and L. A. Santos (2019). Construction of a microbubble generation and measurement unit for use in flotation systems**.** *Chemical Engineering Research and Design* 153.

Braun, M. J. and W. M. Hannon (2010). Cavitation formation and modelling for fluid film bearings: A review. *Proceedings of the Institution of Mechanical Engineers Part J Journal of Engineering Tribology* 224(9), 839-863.

Briggs, L. J. (1950). Limiting negative pressure of water. *Journal of Applied Physics* 21(7), 721-722.

Cai, K., Y. Song, J. Li, D. Wang, J. Yin, W. Liu and L. Hua (2019). Pressure and velocity fluctuation in the numerical simulation of bubble detachment in a venturi-type bubble generator. *Nuclear Technology* 205(1-2), 94-103.

Cui, Y., C. Li, W. Zhang and X. Ning (2022). A deep learning-based image processing method for bubble detection, segmentation, and shape reconstruction in high gas holdup sub-millimeter bubbly flows. *Chemical Engineering Journal* 449, 137859

Deng, X. W., B. Lv, G. Cheng and Y. Lu (2020).

Mechanism of micro/nano-bubble formation and cavitation effect on bubbles size distribution in flotation. *Physicochemical Problems of Mineral Processing* 56(3), 504-512.

Dharmadhikari, A. K., J. A. Dharmadhikari, A. V. Mahulkar, G. Ramanandan, H. Ramachandran, A. B. Pandit and D. Maththur (2011). Dynamics of photothermally created vaporous, gaseous, and mixed microbubbles. *Journal of Physical Chemistry C* 115(14), 6611-6617.

Dilip, C. K. G., V. Anil Kumar, R. K. Gupta, S. V. S. N. Murty and B. P. Kashyap (2018). Effect of strain rate and temperature on the tensile flow behavior and microstructure evolution in Fe-0.3 Pct C-CrMoV grade steel. *Metallurgical and Materials Transactions A.*

Drioli, E. and L. Giorno (2016). Encyclopedia of membranes. *Italy: National Research Council.*

Dular, M. and O. Coutier-Delgosha (2013). Thermodynamic effects during growth and collapse of a single cavitation bubble. *Journal of Fluid Mechanics* 736, 44-66.

Flynn, T. A. and D. R. Deboisblac (1966). *1000 MW Molten Salt Breeder Reactor Conceptual Design Study*. Oak Ridge National Laboratory.

Gordiychuk, A., M. Svanera, S. Benini and P. Poesio (2016). Size distribution and sauter mean diameter of micro bubbles for a venturi type bubble generator. *Experimental Thermal & Fluid Science*70, 51-60.

Huang, J., L. Sun, H. Liu, Z. Mo, J. Tang, G. Xie and M. Du (2020). A review on bubble generation and transportation in venturi-type bubble generators, *Experimental and Computational Multiphase Flow* 2(3), 123-134.

Juwana, W. E., A. Widyatama, O. Dinaryanto, W. Budhijanto and I. Deendarlianto (2018). Hydrodynamic characteristics of the microbubble dissolution in liquid using orifice type microbubble generator. *Chemical Engineering Research and Design*141.

Kawashima, T. H. (2000). Experimental study on microbubbles and their applicability to ships for skin friction reduction. *International Journal of Heat and Fluid Flow*.

Kazakis, N. A., A. A. Mouza and S. V. Paras (2008). Coalescence during bubble formation at two neighbouring pores: An experimental study in microscopic scale. *Chemical Engineering Science* 63(21), 5160-5178.

Kim, Y. B., H. S. Lee and L. Francis (2019). Innovative swirling flow-type microbubble generator for multi-stage DCMD desalination system: Focus on the two-phase flow pattern, bubble size distribution, and its effect on MD performance. *Journal of Membrane Science* 588.

Li, J., Y. Song, J. Yin and D. Wang (2017). Investigation on the effect of geometrical parameters on the performance of a venturi type bubble generator. *Nuclear Engineering and Design* 325, 90-96.

Li, Q., W. Li, J. Zhang, D. Ming and Z. Wang (2020). The effect of ncg on the characteristics of hydraulic cavitation. *Mechanics and Industry* 21(5), 504.

Li, Q., M. Xia, H. L. He , K. C. Yang (2011). Numerical simulation of bubble slip velocity in gas-liquid two-phase flow within horizontal pipe. *Petrochemical Technology* 1000-8144 40:102.0.TX; 2-2.

Li, W., Y. Yang, W. D. Shi, X. Zhao and W. Li (2018). The correction and evaluation of cavitation model considering the thermodynamic effect. *Mathematical Problems in Engineering* 4, 1-11.

Long, Y., X. P. Long, B. Ji, W. X. Huai and Z. D. Qian (2017). Verification and validation of URANS simulations of the turbulent cavitating flow around the hydrofoil. *Journal of Hydrodynamics* 04, 610-620.

Long, Y., X. Long, B. Ji and T. Xing (2019). Verification and validation of large eddy simulation of attached cavitating flow around a clark-y hydrofoil. *International Journal of Multiphase Flow* 115, 93-107.

Nao-Aki, N., Z. Hongfang, T. Kakeru, S. Yoshikazu, T. Yasushi, R. Fei, K. Ryo, U. Toshihiko, Y. Yuji and T. Hiroyuki (2020). Flow characteristics in a honeycomb structure to design nanobubble generating apparatus. *Chemical Engineering & Technology* 43.

Parmar, R. and S. K. Majumder (2013). Microbubble generation and microbubble-aided transport process intensification-A state-of-the-art report. *Chemical Engineering and Processing: Process Intensification* 64, 79-97.

Prosperetti, A (2017). Vapor Bubbles. *Annual Review of Fluid Mechanics* 49(1), 221-248.

Rezai, B. S. B. and S. M. J. Koleini (2008). The studies of effective parameters on bubble size distribution and raise velocity, C. *International Seminar on Mineral Processing*.

Sadatomi, M., A. Kawahara, H. Matsuura and S. Shikatani (2012). Micro-bubble generation rate and bubble dissolution rate into water by a simple multi-fluid mixer with orifice and porous tube. *Experimental Thermal & Fluid Science* 41, 23-30.

Serizawa, A. (2003). Laminarization of micro bubbles containing milky bubbly flow in a pipe. *C. Two-Phase Flow Gr. Meet* 21-27.

Singhal, A. K., M. M. Athavale, H. Li and Y. Jiang (2002). Mathematical basis and validation of

the full cavitation model. *Journal of Fluids Engineering* 124(3), 617-624.

Sun, D., S. Li, C. Fei, Y. T. Ai and R. P. Liem (2019). Investigation of the effect of cavitation and journal whirl on static and dynamic characteristics of journal bearing. *Journal of Mechanical Science & Technology* 33(1), 77-86.

Tabei, K., S. Haruyama, S. Yamaguchi, H. Shirai and F. Takakusagi (2007). Study of micro bubble generation by a swirl jet. *Journal of Environment & Engineering* 2(1), 172-182.

Uchiyama, T., T. Degawa and Y. Kawasaki (2018). Motion of a spherical particle in microbubble plume and bubble behavior around the particle, c. the proceedings of mechanical engineering congress, Japan. *The Japan Society of Mechanical Engineers*.

Wagner, W. (1973). New vapor pressure measurements for argon and nitrogen and a new method for establishing rational vapor pressure equations. *Cryogenics* 13(8), 470-482.

Watarai, N. (2011). Effect of emission conditions of ultrasound in aggregation formation of microbubbles with their specifications. *Ieice Technical Report* 111, 13-18.

Wencai, T., Y. Changqi and S. Licheng (2014). Study on bubble fragmentation characteristics of venturi bubble generator. *Atomic Energy Science and Technology* 5, 81-85.

Wisniak, J. (2001). Historical development of the vapor pressure equation from dalton to antoine, *Journal of Phase Equilibria* 22(6), 622-630.

Yan, Q. S., G. Lu, G. M. Luo, B. W. Xiong and Q. Zheng (2018). Effect of synergistic action of ultrasonic vibration and solidification pressure on tensile properties of vacuum counter-pressure casting aluminum alloy. *China Foundry* 15, 411-417.

Yang, Q., Y. Wang and Z. Zhang (2013). Scale effects on propeller cavitating hydrodynamic and hydroacoustic performances with non-uniform inflow. *Chinese Journal of Mechanical Engineering* 26(2), 414-426.

Yin, J., J. Li, L. Hua, L. Wei and D. Wang (2015). Experimental study on the bubble generation characteristics for an venturi type bubble generator. *International Journal of Heat & Mass Transfer* 91(DEC.), 218-224.

Zhang, F. and H. Li (2020). Visualization of coalescence behavior of two bubbles with smoothness constraint. *Journal of Visualization* 23(3), 475-490.